Simulations of Argon plasmas in the linear plasma device GyM with the SOLPS-ITER code

M Sala[1], E Tonello[1], A Uccello[1,2], X Bonnin[3], D Ricci[2], D Dellasega[1,2], G Granucci[2], M Passoni[1,2]

[1] Politecnico di Milano, Department of Energy, 20133, Milan, Italy
[2] Istituto per la Scienza e Tecnologia dei Plasmi, CNR, 20125, Milan, Italy
[3] ITER Organization, 13067, St Paul Lez Durance, Cedex, France

E-mail: michele.sala@polimi.it

Abstract. Edge plasma codes, such as SOLPS, are widely used to study plasma transport in tokamaks scrape-off layers (SOL). The possibility to apply these codes to non hydrogenic plasmas and to linear plasma devices (LPDs) is gaining the interests of the fusion community. These facilities play a pivotal role in plasma-material interaction (PMI) studies for future fusion devices and may allow to test the code capabilities both in terms of geometry and simulated plasma species. In this contribution, we apply the SOLPS-ITER code for the simulations of Argon plasmas in the medium-flux linear machine GyM. A sensitivity scan over the pumping efficiency, transport coefficients and absorbed electron power was done, performing B2.5-EIRENE coupled simulations. A quantitative analysis of the different flux contributions is provided through the use of a two-point modelling. Comparison with experiments shows a promising qualitative and quantitative agreement, with the sole exception of the simulated neutrals pressure. Dedicated EIRENE standalone simulations were performed to investigate this issue, also highlighting the role of neutral-neutral elastic collisions at high values of the puffing intensity.

1. Introduction

Starting from the Nineties, increasingly advanced computational models have been developed with the purpose to numerically study the plasma transport in the edge region of magnetic fusion devices. In particular, codes such as SOLPS [1] and SOLEDGE2D-EIRENE [2] include a state-of-the-art treatment of plasma transport along and across magnetic field lines as well as a complete treatment of atomic processes occurring in the plasma edge. The feature that makes these codes highly relevant for boundary plasma modelling is the possibility to simulate in great detail the interaction of the plasma with the neutral particles. Neutral atoms and molecules are present in the boundary plasma due to the recycling from the plasma facing materials (PFMs) and for seeding purposes. They are based on the so-called mean-field approach [3] and as a downside, they do not include turbulence self-consistently in the model, although some recent studies were done in that direction [4, 5, 6]. The latest applications of these kind of codes are about the study of the effect different PFMs [7], the modelling of divertor closure [8] and Ne and N seeding effects [9, 10].

In spite of the fact that edge plasma codes have been developed with reference to the toroidal geometry of a tokamak, the possibility to numerically simulate plasmas in linear plasma devices (LPDs) is of great interest due to the pivotal importance of these devices in plasma-material interaction (PMI) studies. Indeed, experimental investigations of PMI in ITER-relevant conditions have been widely performed in LPDs [11, 12]. The relatively simple configuration of these devices offers the possibility to build cost-effective facilities to address aspects of key importance for controlled magnetic fusion, such as divertor detachment and materials testing in the high-flux and fluence conditions foreseen in ITER and DEMO. However, interpretation of the results of these experiments often relies on plasma quantities which are not easy to be measured: an example can be plasma composition, in terms of chemical aggregation and the ionisation degree of each isotope. Such properties may in principle be easily recovered from numerical simulations. Furthermore, the simulation of LPDs with the most advanced and complex numerical codes for tokamaks is not without challenges.

So far, simulations of LPDs using edge plasma codes have been concerned in interpretative as well as predictive studies [13, 14, 15, 16, 17, 18, 19, 20]. In particular, Kastelewicz et al. [13] are the first that applied SOLPS4.0 to a linear geometry. They showed the structure of a computational grid for LPD simulations and gave a description of the type of boundary conditions to be used in linear geometry. The same SOLPS version was used in [14] for predicting the main plasma parameters in MAGNUM-PSI. More recent works used SOLPS5.0 to simulate plasma transport in MAGPIE [18] and PROTO-MPEX [16, 17]. In particular, Rapp et al. [15] were the first to describe how to model radio-frequency heated LPDs with SOLPS. The SOLEDGE2D-EIRENE code was applied to PILOT-PSI to understand the effects of different atomic physics models [20]. Effects of pumping efficiency and radial transport coefficients were studied [19] and a quantitative analysis of the importance of transport and atomic processes, based on the two-point model [21, 22], was performed. Alongside the efforts to adapt tokamak mean-field edge codes to LPDs, some attempts were also made to develop codes which implement plasma transport models in cylindrical geometry, both considering mean-field transport questions [23, 24, 25, 26, 27] and a consistent treatment of turbulence [28, 29, 30, 31, 32]. While this approach allows simplifications in the transport equations due to a simpler geometry, these codes are presently limited due to the absence or the highly simplified treatment of neutral species and their interactions with the background plasma.

In this work, we perform a first investigation towards the integrated simulations of PMI experiments in LPDs. We focus, in particular, on the plasma side of the problem, using the latest released version of the SOLPS code, namely SOLPS-ITER, for simulating pure argon (Ar) plasma in the LPD GyM of Istituto di Scienza e Tecnologia dei Plasmi (ISTP)-CNR. This machine, originally designed with the aim of studying basic plasma physics, such as plasma turbulence [33], is now mainly used to study plasma-wall interaction for fusion applications [34].

To the best of our knowledge, this work is the first application of SOLPS-ITER to a LPD and it is the first time this code is used to simulate non hydrogen-dominated plasmas. The choice to consider pure Ar plasma is unusual for simulations with edge transport codes, where hydrogen (H) or deuterium (D) are commonly the main plasma species. Indeed, in

tokamaks, Ar impurities are present in trace in the plasma as seeding for power dissipation purposes [35, 36]. In PMI studies performed in LPDs, instead, Ar is often selected as the main plasma species [37, 38].

In section § 2, we show how plasma transport equations are modified for the simulation of Ar plasma in LPDs. After illustrating the main aspects of GyM (section § 3) and the simulation inputs (section § 4), in section § 5, we present and discuss the main results of this work. We investigated the effects of some code free parameters on the plasma profiles and we interpreted the results of these simulations using a two-point modelling analysis, akin to that presented in [20]. A first comparison with available experimental plasma profiles is then showed. Finally, results of EIRENE standalone simulations are presented.

2. The numerical model

2.1. SOLPS-ITER modelling of LPDs

SOLPS [1] is a suite of codes for the simulations of tokamak edge plasmas. The two most important packages are B2.5 and EIRENE. The former solves a set of 2D coupled conservation equations in curvilinear coordinates which describe the electron and atomic ion populations as a collection of mutually interacting fluids. The latter [39] is a 3D kinetic code which computes the transport of atomic and molecular neutral species onto a given plasma background.

The two codes can be used separately, in the so-called standalone mode, or may be coupled iteratively. In the latter case, B2.5 solves the plasma fluid equations (continuity equations for the average plasma density n, electron and ion temperature, T_e and T_i, ion momentum and current density). The information of the plasma background is then passed to EIRENE, which computes Monte Carlo history of neutral particles and, if present, also the molecular ions. Their interactions with the plasma background are computed and the corresponding source terms are then passed to the B2.5 fluid equations. This scheme is repeated iteratively to reach convergence of the code.

The B2.5 equations are specifically tailored for tokamaks simulations and written in a curvilinear orthogonal coordinate system, as described in [40]. In figure 1, we show the two reference frames considered to write B2.5 equations: the *dynamical reference frame* $(\mathbf{e}_\parallel, \mathbf{e}_\perp, \mathbf{e}_y)$, aligned with the characteristic directions of the plasma motion, and the *geometrical reference frame* $(\mathbf{e}_x, \mathbf{e}_y, \mathbf{e}_z)$. Exploiting the rotational symmetry of the tokamak in the toroidal direction $\mathbf{e}_z$, the problem can be reduced to two-dimensional in the geometrical reference frame. In this frame, the metric is diagonal and entirely described by the three metric coefficients h_x, h_y, h_z. The x-coordinate varies along the flux surfaces, while the y-coordinate is perpendicular to them. The application of SOLPS to LPDs is not straightforward due to the coordinate system implemented in the code. In figure 1, we describe how the x, y and z directions of the geometrical frame have to be interpreted when a linear geometry is considered. Again, the problem can be reduced to 2D exploiting rotational symmetry around the cylinder axis. The $\mathbf{e}_z$ basis vector in linear geometry is along the polar direction and the bi-dimensional problem is solved on the plane parallel to the cylinder axis. Specifically, the x-coordinate corresponds to the axial direction and the y-coordinate is in the radial direction.
The general transformation rules of a vector $\mathbf{v}$ from the dynamical frame to the geometrical one, derived in [40], for a linear plasma device reduce to:

$$v_x = b_x v_\parallel \qquad v_z = -b_x v_\perp \tag{1}$$

where $b_x = B_x/B$. The relations are obtained by setting to zero the polar component of the magnetic field $b_z = B_z/B = 0$. Indeed, a major difference, when using the code to simulate a LPD, is the absence of the polar component of the magnetic field B_z, which is instead the dominant component in tokamaks. This eliminates several terms in SOLPS-ITER equations, mainly related to the possibility to investigate drifts.

2.2. The B2.5 equations for Ar plasmas in LPDs

In this section, we discuss the form taken by the B2.5 equations with the setup used for the simulations performed in this work. It should be noted that these equations, originally presented in [41], were derived aiming to simulate hydrogen-dominated plasmas, in which heavier species such as Ar are treated as impurities. Anyway, the latest version of SOLPS-ITER physics model is based on the Zhdanov formulation [42] for the transport coefficients. The resulting equations can be used also in the case of non hydrogen-dominated plasmas, provided that only a single ion charge state is considered. In our simulations, the plasma is composed by the electron population, a single-charged ion population Ar^+ and the Ar neutral population (cfr. section § 4). The ion continuity equation becomes

$$\partial_t n + \frac{1}{\sqrt{g}}\partial_x\left(\frac{\sqrt{g}}{h_x} n b_x v_\parallel\right) + \frac{1}{\sqrt{g}}\partial_y\left(\frac{\sqrt{g}}{h_y} n v_y\right) = S^n_{n,i} \tag{2}$$

where the source term $S^n_{n,i}$ is due to ionisation, recombination and charge exchange reactions with neutral Ar atoms.

In the radial direction, a diffusive ansatz is used to determine the y component of the ion velocity:

$$v_y = -D^{\text{an}}_n \frac{1}{h_y n}\partial_y n - D^{\text{an}}_p \frac{1}{n h_y}\partial_y p_i \tag{3}$$

Here D^{an}_n and D^{an}_p are anomalous transport coefficients. Their values are free parameters for the code

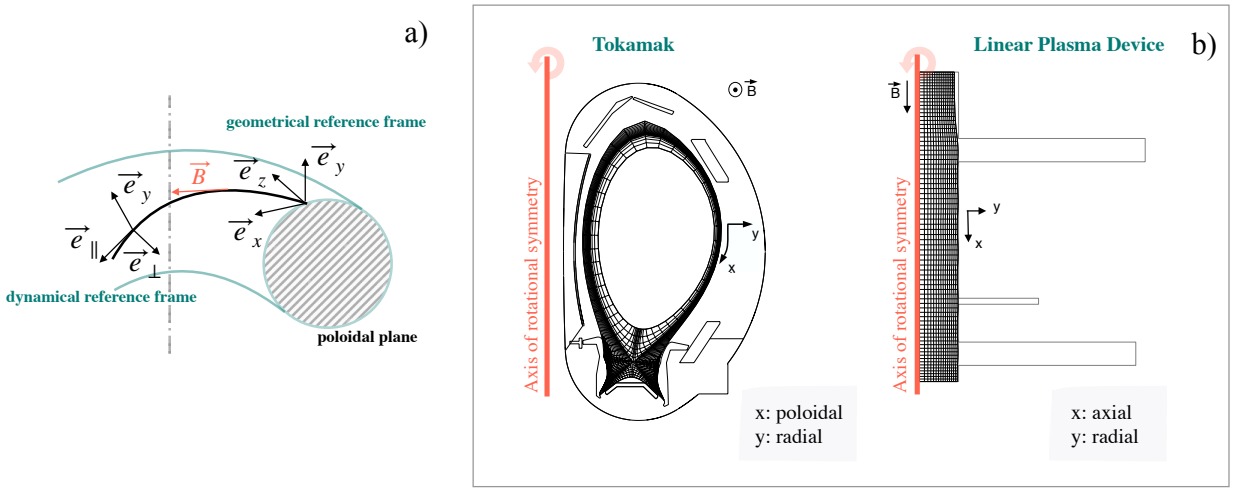

Figure 1. a) Curvilinear reference frames of B2.5. The *dynamical reference frame* $(\mathbf{e}_\parallel, \mathbf{e}_\perp, \mathbf{e}_y)$ is aligned to the characteristic directions of the plasma motion: parallel to the magnetic field $\mathbf{B}$ ($\mathbf{e}_\parallel$) and orthogonal to $\mathbf{B}$ in the magnetic flux surface ($\mathbf{e}_\perp$); the third direction is orthogonal to the magnetic flux surfaces ($\mathbf{e}_y$). The *geometrical reference frame* $(\mathbf{e}_x, \mathbf{e}_y, \mathbf{e}_z)$, where $\mathbf{e}_x$ is in the poloidal direction, $\mathbf{e}_y$ is orthogonal to the flux surfaces in the poloidal plane and $\mathbf{e}_z$ is in the toroidal direction. For a complete derivation of the plasma transport equations in these two curvilinear reference frames refer to [40]. **b)** Geometrical reference frame conversion from a tokamak to a LPD. In both cases the z direction can be ignored, assuming rotational symmetry around the axis reported in red.

and they are used to reproduce the averaged transport effects of turbulence. The parallel electron velocity is computed as $v_\parallel - j_\parallel/(en)$. Similarly, in the radial direction, we obtain the electron velocity as $v_y - j_y/(en)$. This assumes that the current is fully carried by the electrons. See below, equations (14) and (15), for the definition of the current components. The electron density is obtained from quasi-neutrality, i.e. in our case is equal to the Ar^+ density everywhere.

The parallel ion velocity, $v_\parallel$, is obtained by solving the parallel ion momentum equation. For the simulations performed in this work, it is given by:

$$\begin{aligned} m_i\Bigg[\partial_t\left(nv_\parallel\right) + \frac{1}{h_z\sqrt{g}}\partial_x\left(\frac{\sqrt{g}h_z}{h_x}nb_x v_\parallel^2\right) + \\ + \frac{1}{h_z\sqrt{g}}\partial_y\left(\frac{\sqrt{g}h_z}{h_y}nv_\parallel v_y\right)\Bigg] = -\frac{b_x}{h_x}en\partial_x\phi - \\ - \frac{b_x}{h_x}\partial_x\left(nT_i\right) + \frac{1}{h_z\sqrt{g}}\partial_x\left(\frac{\sqrt{g}h_z}{h_x^2}\eta_{ix}\partial_x v_\parallel\right) + \\ + \frac{1}{h_z\sqrt{g}}\partial_y\left(\frac{\sqrt{g}h_z}{h_y^2}\eta_{iy}\partial_y v_\parallel\right) + S^m_{n,i} + S^m_{\mathrm{fr}_{ie}} + S^m_{\mathrm{therm}_{ie}} \end{aligned} \tag{4}$$

where η_{ix} and η_{iy} are the axial and radial ion viscosity coefficients, respectively. Here, $\eta_{ix} = \eta^{an} + \eta^{cl}$ and $\eta_{iy} = \eta^{an}$, where η^{cl} is the Zhdanov classical viscosity coefficient [42] while the anomalous contribution is related to the anomalous diffusion coefficient D_n^{an} according to $\eta^{an} = m_i n D_n^{\mathrm{an}}$ [43]. $S^m_{n,i}$ represents the momentum source due to ion-neutral friction computed by EIRENE, $S^m_{\mathrm{fr}_{ie}}$ is the electron-ion friction force and $S^m_{\mathrm{therm}_{ie}}$ is the electron-ion thermal force, whose expressions are reported in [44].

The energy balance equation for the electron is:

$$\begin{aligned} \frac{3}{2}\partial_t\left(nT_e\right) + \frac{1}{\sqrt{g}}\partial_x\left(\frac{\sqrt{g}}{h_x}\tilde{q}_{ex}\right) + \frac{1}{\sqrt{g}}\partial_y\left(\frac{\sqrt{g}}{h_y}\tilde{q}_{ey}\right) + \\ + \frac{nT_e}{\sqrt{g}}\partial_x\left(\frac{\sqrt{g}}{h_x}b_x\left(v_\parallel - \frac{j_\parallel}{en}\right)\right) = \\ = Q_\Delta + Q_{\mathrm{fr,therm}} + Q_{n,e} + Q_R \end{aligned} \tag{5}$$

where

$$\tilde{q}_{ex} = \frac{3}{2}nT_e b_x\left(v_\parallel - \frac{j_\parallel}{en}\right) - \kappa_{e\parallel}\frac{b_x^2}{h_x}\partial_x T_e \tag{6}$$

and

$$\begin{aligned} \tilde{q}_{ey} = \frac{5}{2}nT_e\Bigg(-D_n^{\mathrm{an}}\frac{1}{nh_y}\partial_y n - D_p^{\mathrm{an}}\frac{1}{nh_y}\partial_y p_i\Bigg) - \\ - \kappa_{e\perp}\frac{1}{h_y}\partial_y T_e \end{aligned} \tag{7}$$

Here $\kappa_{e\parallel}$ and $\kappa_{e\perp} = \chi_e^{\mathrm{an}} n$ are respectively the Zhdanov thermal conductivity [42] and the anomalous one for electrons. The electron energy sources on RHS of equation 5 are:

- the electron-ion energy equipartition, Q_Δ:

$$Q_\Delta = \nu_{ei}\left(T_e - T_i\right) \tag{8}$$

where ν_{ei} is the electron-ion collision frequency.

- the heat source from electron-ion friction and thermal forces, which is proportional to the electron velocity:

$$Q_{\mathrm{fr,therm}} = \left(S^m_{\mathrm{fr}_{ie}} + S^m_{\mathrm{therm}_{ie}}\right)\left(\frac{j_\parallel}{en} - v_\parallel\right) \tag{9}$$

- $Q_{n,e}$ and Q_R are the electron energy sources due to interactions of electrons with neutral Ar atoms and Ar^+ ions, respectively.

Analogously, the ion energy equation can be written as:

$$\begin{aligned}\frac{3}{2}\partial_t\left(nT_i\right) + \frac{1}{\sqrt{g}}\partial_x\left(\frac{\sqrt{g}}{h_x}\tilde{q}_{ix}\right) + \frac{1}{\sqrt{g}}\partial_y\left(\frac{\sqrt{g}}{h_y}\tilde{q}_{iy}\right) + \\ + \frac{nT_i}{\sqrt{g}}\partial_x\left(\frac{\sqrt{g}}{h_x}b_x v_\parallel\right) = Q_\Delta + Q_{n,i} \\ + \eta_{ix}\left(\frac{\partial_x v_\parallel}{h_x}\right)^2 + \eta_{iy}\left(\frac{\partial_y v_\parallel}{h_y}\right)^2\end{aligned} \tag{10}$$

The ion energy fluxes, $\tilde{q}_{ix}$ and $\tilde{q}_{iy}$, are given by:

$$\tilde{q}_{ix} = \frac{3}{2}nT_i b_x v_\parallel - \kappa_{i\parallel}\frac{b_x^2}{h_x}\partial_x T_i \tag{11}$$

and

$$\begin{aligned}\tilde{q}_{iy} = \frac{5}{2}nT_i\left(-D_n^{\mathrm{an}}\frac{1}{nh_y}\partial_y n - D_p^{\mathrm{an}}\frac{1}{nh_y}\partial_y p_i\right) - \\ - \kappa_{i\perp}\frac{1}{h_y}\partial_y T_i\end{aligned} \tag{12}$$

where $\kappa_{i\parallel}$ and $\kappa_{i\perp} = \chi_i^{\mathrm{an}} n$ are respectively the classical thermal conductivity and the anomalous one for Ar^+ ions. The electrostatic potential ϕ can be derived from the current continuity equation. In the (x, y, z) coordinate system it is given by:

$$\frac{1}{\sqrt{g}}\partial_x\left(\frac{\sqrt{g}}{h_x}b_x j_\parallel\right) + \frac{1}{\sqrt{g}}\partial_y\left(\frac{\sqrt{g}}{h_y}j_y\right) = 0 \tag{13}$$

The parallel component of the current density, $j_\parallel$, can be obtained from the electron momentum equation (generalised Ohm's law) and it is given by:

$$j_\parallel = \sigma_\parallel\left[\frac{b_x}{e}\frac{1}{n}\frac{1}{h_x}\partial_x\left(nT_e\right) - \frac{b_x}{h_x}\partial_x\phi\right] - \alpha_{ex}\frac{1}{h_x}\partial_x T_e \tag{14}$$

where the parallel electrical conductivity $\sigma_\parallel$ and the classical thermo-electric coefficient α_{ex} are expressed according to Zhdanov formulation [42].

The radial component of the current density, j_y, accounts only for the anomalous current, j_y^{an}, which reads

$$j_y = j_y^{\mathrm{an}} = -\sigma^{\mathrm{an}}\frac{1}{h_y}\partial_y\phi \tag{15}$$

and $\sigma_{\mathrm{an}} = k_{\mathrm{an}} en$ is the anomalous conductivity. Non vanishing σ_{an} is needed to provide convergence of the numerical scheme, as reported in [45]. In these simulations, the value of k_{an} was set to 1×10^{-6}.

3. The linear plasma device GyM

In this section, the linear plasma device GyM is shortly described. The emphasis is here given to the aspects of relevance for the simulations.

GyM structure is shown in figure 2. The main chamber consists of a cylindrical stainless steel vacuum vessel of 0.25 m diameter and 2.11 m length surrounded by 10 magnetic coils. From figure 2, we can see the location of the two radiofrequency (RF) sources delivering up to 3.0 kW and 1.5 kW, the Langmuir Probe (LP), the gas injection nozzle, the two turbomolecular pumps and the pressure gauge. The main experimental Ar plasma parameters are reported in table 1.

The standard magnetic configuration in GyM is obtained connecting all the 10 coils in series, so that the same current flows in each of them. The resulting magnetic field is directed along the cylinder axis and its intensity is modulated by changing the axial coil distance. The peak magnetic field can reach the value of about 0.13 T. The magnetic field is obtained by solving the Grad-Shafranov equation [46]:

$$\Delta^* \psi = -\mu_0 R J_z \tag{16}$$

where ψ is the flux function, μ_0 the vacuum magnetic permeability, R is the radius. J_z is the azimuthal current density and it includes contributions coming from the plasma and from the external magnetic field coils. In a LPD, the plasma current can be neglected with respect to the one flowing in the external magnetic field coils. The stream-function ψ resulting from the solution of equation (16) for GyM, considering a coil current of 600 A is shown in figure 3.

The plasma in GyM is generated and sustained exploiting the electron cyclotron resonance (ECR) heating mechanism at 2.45 GHz, which directly heats only the electron population. This, in combination with the relatively low plasma density, results in a cold ion population ($\lesssim 0.1$ eV) in the plasma. Among the two RF sources installed on the machine, here we will consider only the one which can deliver up to 3.0kW. As shown in figure 2, this is connected to the vessel through a waveguide. In figure 4, we show the location on the (Z, R) plane of the ECR region in GyM for different values of the coil current or, equivalently, for

Table 1. Typical working conditions for Ar plasma in GyM. The main plasma parameters are measured by Langmuir Probes.

GyM reference conditions	
Neutral pressure	$10^{-5} - 10^{-4}$ mbar
Plasma density	$10^{16} - 10^{17}$ m^{-3}
Electron temperature	$5 - 10$ eV
Flux density	up to 10^{21} m^{-2}s^{-1}
Fluence	up to 10^{25} m^{-2}

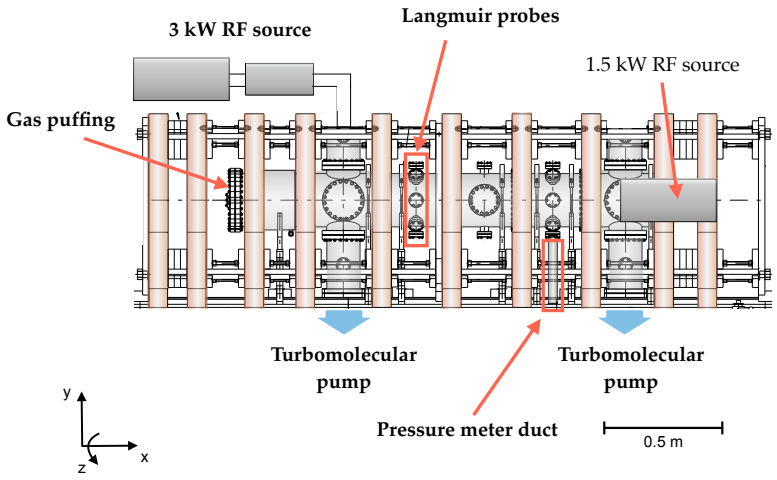

Figure 2. Schematic drawing of GyM linear machine with the magnetic field coils and the vacuum chamber. The Langmuir Probe (LP) location, the RF sources at 2.45 GHz capable of delivering up to 4.5 kW and the gas nozzle located at one end of the cylindrical vacuum vessel are shown. The 1.5 kW RF source is reported in figure, but it will not be considered in the following.

different values of B. In this work we will consider the magnetic field configuration corresponding to 600 A, for which the ECR is located around a very narrow axial region. Additional resonances might be present in the machine, related to the upper-hybrid branch of the dispersion relation. Their location in the machine is, however, difficult to predict, since they depend on the local plasma density, which is not known a priori. For this reason, in this first work we neglect the presence of such additional resonances. Furthermore, direct measurements of the EC absorbed power are not available at present for the plasma of GyM, which point towards the interest in the parametric scan as described in section § 5.

The experimental plasma parameters (n, T_e and ϕ) were obtained by means of a Langmuir probe (LP), located $\sim$ 30 cm in front of the 3.0 kW RF source, as shown in figure 2. The stainless steel probe tip is cylindrical (1cm length and 1.5mm diameter) and it is mounted on a movable shaft so that its radial position can be varied to record the radial profile of plasma parameters.

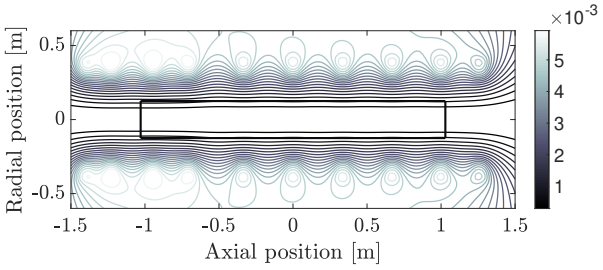

Figure 3. Contour lines of the stream-function ψ in $[\mathrm{T\,m^2}]$ for GyM standard coil configuration at 600 A. The solid black lines mark the GyM vacuum vessel.

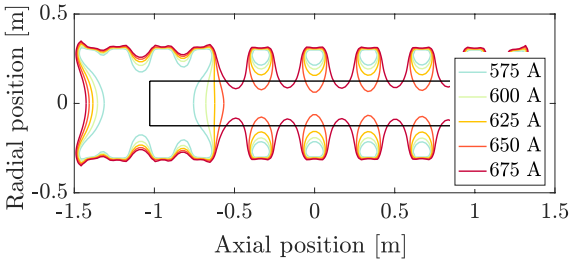

Figure 4. ECR location for different values of B or, equivalently, current in the coils.

4. Simulation setup

The most basic inputs of SOLPS-ITER are the two computational grids, one for B2.5 and one for EIRENE. B2.5 works with a structured curvilinear quasi-orthogonal mesh. This is made of quadrilateral cells with two sides parallel to the magnetic flux surfaces and two in the radial direction. This is consistent with the decomposition of plasma flow in the direction along and across the magnetic flux surfaces. The EIRENE grid is made of triangles and is constructed starting from the B2.5 fluid grid. Since neutrals are present also outside the plasma, this grid covers the whole cross-section of the machine, including

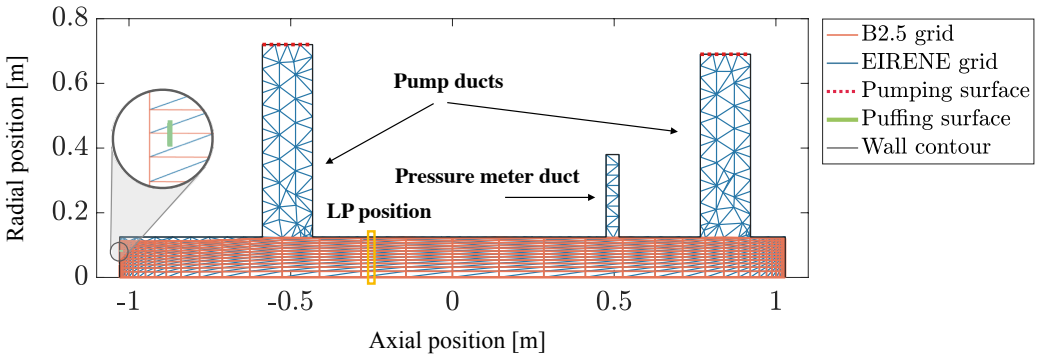

Figure 5. GyM computational grids for B2.5-EIRENE simulations. The EIRENE grid covers also the whole 2D cross-section of the device, including the pumps and the pressure meter ducts. The pumping surfaces are shown in dotted red and the puffing surface in green, in correspondence of the west target.

secondary ducts outside the cylindrical chamber. To build the field-aligned computational grid for B2.5 it was first necessary to construct the equilibrium magnetic field by solving equation (16). The contour lines of the stream-function, shown in figure 3, were then used to obtain the mesh. A constrain imposed by B2.5 is to limit the grid radially to a certain outermost surface of constant magnetic flux, rather then extend it through the true chamber wall [47]. It is common to refer to this outer radial boundary as the north boundary of the mesh. The result is shown by orange lines in figure 5. The EIRENE grid includes the pump and the pressure meter ducts, as shown by blue lines in figure 5. Although in EIRENE it is possible to implement a full 3D mesh to take into account geometry asymmetries, in this first work we assumed azimuthal symmetry around the x-coordinate. In this way, the volume of the ducts departing from the main cylindrical chamber is bigger than the real physical volume. In figure 5, we also show the pumping and puffing surfaces.

Pumping is accounted for by prescribing in EIRENE an absorption probability for neutrals on given pumping surfaces. The absorption probability p_a, or *albedo* of the surface, is related to the particle recycling coefficient RECYCT by $p_a = (1 - \text{RECYCT})$. Finally, the puffing surface, which in the experimental setup is on one of the two targets (cylinder basis), is inside the west boundary of the plasma grid and required some care to be implemented in the code. A dedicated transparent surface was included in EIRENE grid (shown in green in the inset in figure 5), from which we prescribed the puffing strength.

Radial transport is largely dominated by turbulence, which cannot be modelled self-consistently in SOLPS. For this reason, a diffusive ansatz for the turbulent flux is usually adopted, where the values of the diffusion coefficients are treated as free parameters and are adjusted to match experimentally measured plasma profiles.

Table 2. Radial transport coefficients, pumping albedos and overall absorbed electron power considered in this work.

Case	$D_n^{\text{an}}, D_p^{\text{an}}$ $[\text{m}^{-2}\text{s}^{-1}]$	$\chi_e^{\text{an}}, \chi_i^{\text{an}}$ $[\text{m}^{-2}\text{s}^{-1}]$	P^{ext} [W]	RECYCT
(a)	1.5	1.5	800	0.985
(b)	1.5	1.5	800	0.970
(c)	1.5	1.5	800	0.990
(d)	0.5	1.5	800	0.985
(e)	2.5	1.5	800	0.985
(f)	1.5	1.5	2400	0.985

The power delivered by the RF source was modelled as an additional, user-prescribed, term in the electron energy equation. A precise description of the overall power delivered to the plasma as well as the knowledge of the spatial distribution of the power density require a dedicated study, and it is beyond the scope of the present article. In this contribution, we assume that the power density is constant in the radial direction and Gaussian distributed in the axial direction, that is:

$$S_e^{\text{ext}} = P^{\text{ext}} \exp\left[-\frac{(z - z_{\text{res}})^2}{\sigma^2}\right] \tag{17}$$

The mean value, z_{res}, of the Gaussian is fixed at the theoretical resonance location and the variance, σ^2, is fixed to 0.1 m. The overall power delivered by the source and actually absorbed by the electron population, P^{ext}, is treated as a free parameter, since it is not currently experimentally measured, as mentioned in § 3. In this work, a sensitivity study of the impact of the pumping efficiency, radial transport

coefficients and external power is presented, according to the scheme detailed in table 2.

As regards the boundary conditions, at the two targets location, standard Bohm sheath conditions were set. On the axis of symmetry (i.e. the machine axis), we assumed vanishing fluxes of all the plasma parameters. Finally, at the north boundary of the B2.5 simulation domain we imposed a prescribed value for the decay lengths of the plasma parameters: $\lambda_{n_e} = 0.05\,\mathrm{m}, \lambda_{T_e} = 0.05\,\mathrm{m}, \lambda_\phi = 0.1\,\mathrm{m}$ and $\lambda_{T_i} = 0.1\,\mathrm{m}$ for the electron density, electron temperature, plasma potential and ion temperature. For the momentum equation, we assumed instead a vanishing value for the parallel momentum flux.

Due to the low plasma density ($\sim 10^{17}\mathrm{m}^{-3}$), the mean free path expected for Coulomb collisions among electrons and ions in Gym is comparable with the characteristic length of the device. The fluid equations implemented in B2.5 are derived for the high-collisionality limit and, strictly speaking, should not be applied in such low collisionality regime. For this reason, kinetic corrections to the parallel transport coefficients are to be taken into account [21]. This is done in SOLPS by adding flux limits to the electron and ion fluxes [48]. The value for the electron and ions heat flux limit was set to 0.15, while viscosity, thermo-electric coefficient and friction force flux limits are set to reference value 0.5. The effect of different values of flux limits was also evaluated and it was found to be negligible.

Finally, for all the simulations that we performed, the following set of Ar reactions were included:

$$e^- + \mathrm{Ar} \rightarrow \mathrm{Ar}^+ + 2e^-$$
$$e^- + \mathrm{Ar}^+ \rightarrow \mathrm{Ar}$$

Elastic scattering between Ar and Ar^+ was not considered in this work, since the corresponding reaction rates are not included in the available EIRENE databases. All the remaining charge states, from Ar^{2+} to Ar^{18+}, were also neglected. Indeed, the electron temperature in GyM is rather low (below 8 eV). This, in combination with the low electron density (below $10^{17}\,\mathrm{m}^{-3}$), leads to a low probability for the ionisation of the higher Ar charge states. The validity of this assumption was also checked with a dedicated simulation where the Ar^{2+} was included, using the same input as for case *a*) of table 2, observing that the ratio $n_{\mathrm{Ar}^{2+}}/n_{\mathrm{Ar}^+} \sim 0.1$.

5. Results and discussion

5.1. B2.5-EIRENE coupled simulations

An analysis of the effects of the absorbed electron power, transport coefficients and pumping efficiency was performed using the B2.5-EIRENE coupled version of the code. Simulated radial profiles of n, T_e, ϕ and T_i at the axial position of the Langmuir Probe are shown in figure 6. The details of the simulations are reported in table 2. Case *a*) is the reference one. *b*) and *c*)(orange curves in figure 6) show the effect of a lower and higher RECYCT, respectively. Cases *d*) and *e*) (green curves in figure 6) do the same for the particle diffusion coefficients, D_n^{an} and D_p^{an}. Many transport codes, such as SOLPS, approximate turbulent transport via effective diffusion of particles (D_n^{an} and D_p^{an}) and heat ($\kappa_{e\perp} = \chi_e^{\mathrm{an}} n$ and $\kappa_{i\perp} = \chi_i^{\mathrm{an}} n$). The values of the anomalous transport coefficients are free parameters of the code, used to match the experimental radial profiles [49]. In our simulations the effects of the particle diffusion was evaluated varying D_n^{an} and D_p^{an}, while the heat diffusivity coefficients χ_e^{an} and χ_i^{an} were fixed at constant values. Finally, case *f*) shows the effects of an increased absorbed electron power. First of all, it can be noted that for all our simulations radial profiles show a rather similar behaviour. The electron density is a monotonic function of the radial position, peaked at the machine axis and slowly decreasing towards the vessel chamber. Electron temperature and plasma potential share a similar profile: they peak near the vessel boundary, where the n is lower. The T_e profile resulting from the simulations is seen to be strictly influenced by the electron power distribution given as input [18]. In our case, the source is a RF magnetron and the heating mechanism is by electron cyclotron resonance. We guessed a power density, which is radially constant with a Gaussian profile along the axis. This allows to obtain the SOLPS radial T_e profiles of figure 6 which increase along R. To demonstrate that the power density given as input to the code primarily determines the T_e profile, simulations with a different modelling of the source were carried out. We found that, for a radially Gaussian peaked at the cylinder axis, the T_e profile monotonically decreases with R. The similarity between T_e and ϕ profiles can be understood by considering that, under radial ambipolarity conditions, $j_y = 0$, the following expression can be obtained for Ar plasmas $\phi(r) = 4.6\, k_b T_e(r)/e$ [21]. This relationship has indeed be checked for the simulated profiles, showing that the σ_{an} is low enough not to influence the final simulation result.

Cases *a*), *b*) and *c*) were performed changing only the value of the recycling coefficients of the pumping surfaces. It can be noted that this parameter has a great impact on the simulated radial profiles. For the lowest value, case *b*), of the recycling coefficient (that is, when the neutrals absorption probability is the highest) n reduces significantly, while T_e and ϕ increase, with respect to case *a*). This can be reasonably understood as due to the fact that the

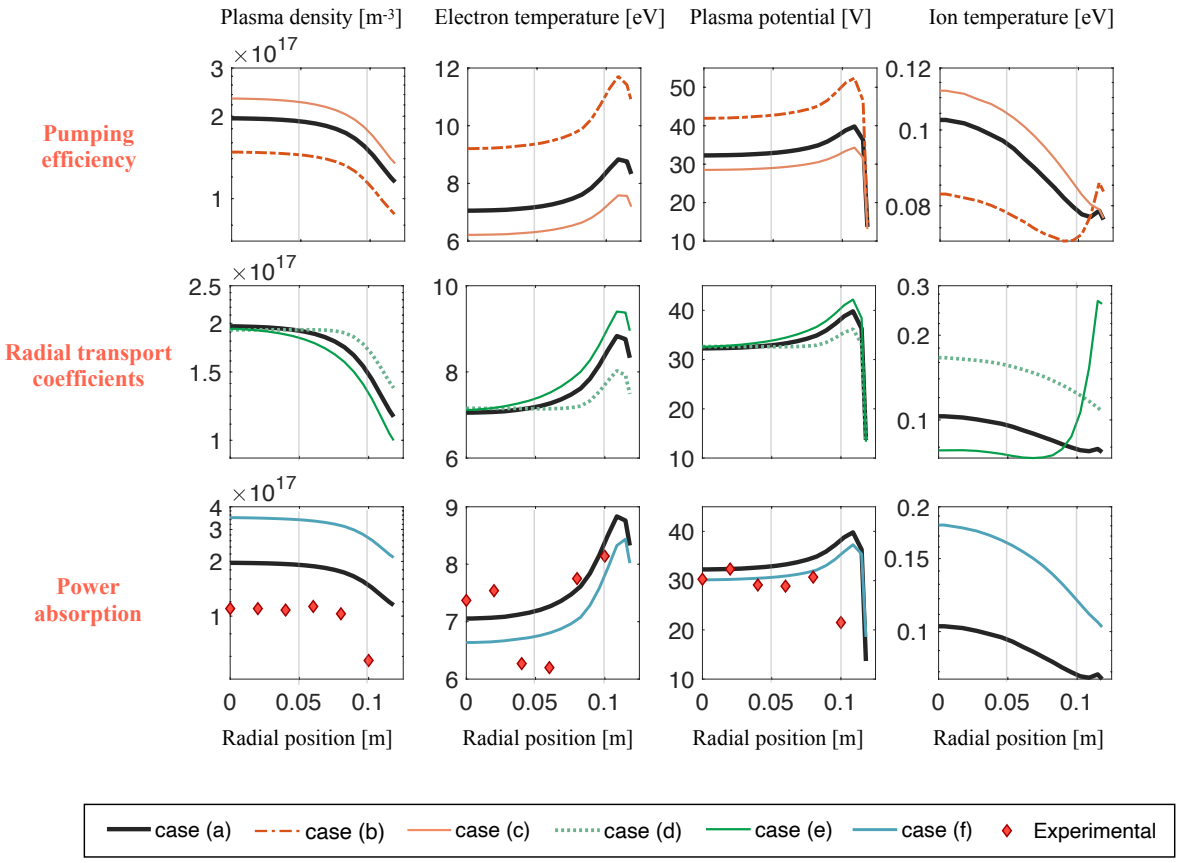

Figure 6. Effects of the neutral pumping efficiency (top), radial transport coefficients (middle) and absorbed power (bottom) on the simulated radial profiles of the electron density, electron and ion temperature, and plasma potential. Different colors and line styles correspond to the the different cases in 2. The profiles extend from the machine axis ($y = 0$) to the lateral side of the cylinder ($y = 0, 125\,\mathrm{m}$). The axial position at which radial profiles are taken correspond to that of the LP (see figure 5).

amount of power delivered is equal for all the three cases, but the neutrals in the system is lower in case b) and highest in case c). For case c), thus, the energy absorbed by the electrons due to the external RF source is quickly lost by ionisation of neutrals, whose density is higher for case c). As a consequence of the increased electron density, one can notice that the ion temperature also slightly increases for case c). Since ions are not directly heated by the RF source, their only relevant energy source comes from electron-ion collisions (energy equipartition), whose frequency scales proportionally to the plasma density.

In cases $a), d)$ and $e)$ only the radial diffusion coefficients where varied. D_n^{an} and D_p^{an} were varied simultaneously, so that the overall effect of radial particle diffusion is taken into account. Comparing the black and green lines in figure 6, one can notice that the greatest impact of this parameter is on the shape of the simulated radial profiles, while the values of electron density, temperature and plasma potential at the axis are left unchanged. In particular, n is almost flat up to larger radial positions when the radial transport coefficients are lower - case d), and T_e and ϕ maxima reach lower values. For higher diffusion coefficients - case e), the opposite trend is obtained, consistently with the fact that a larger number of particles is removed radially.

Cases a) and f) show the effect on the plasma solutions of an increased power absorbed by the electron population. One can notice that, as a consequence of external power variations, the strongest impact is on the electron density, while the electron temperature and plasma potential are almost unchanged. A rise in the plasma density as a consequence of an increased ECR heating power can be understood as due to the fact that, with a fixed amount of neutrals in the system, the excess in the electron energy is efficiently dissipated in collisions with Ar atoms leading to their ionisation. This is consistent since the overall degree of ionisation in the

GyM plasma is rather low.

5.2. Two-point analysis of the simulations results

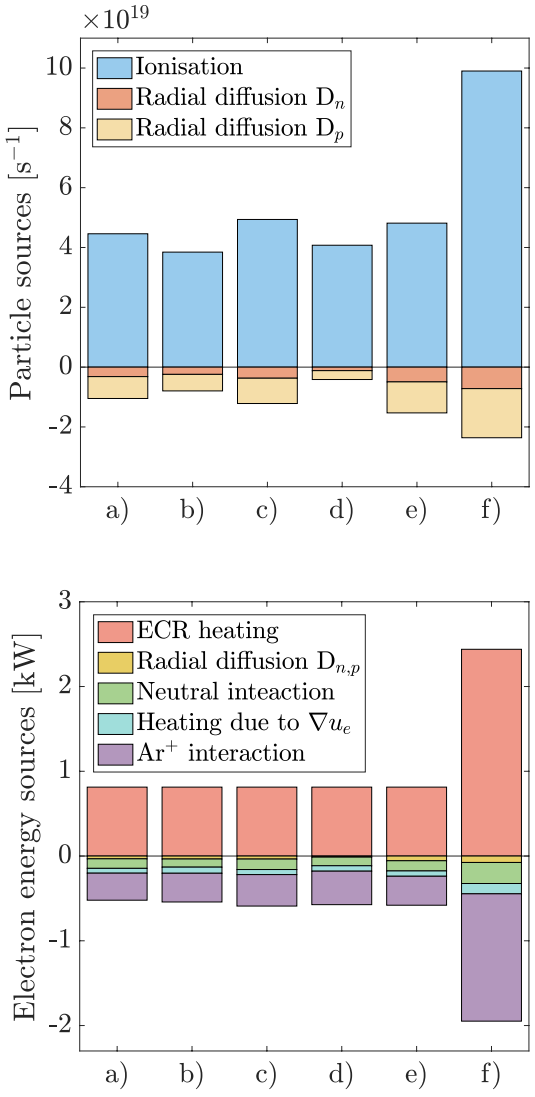

Figure 7. Particle (top) and electron energy (bottom) source terms for the cases reported in table 2. The Ar^+ interaction term in the graph at the bottom is an effective ion recombination rate.

To provide additional physical insight to the analysis performed in section 5.1, here we present a two-point analysis based on the SOLPS-ITER equations [21, 19]. Here, we integrate the steady state density and electron temperature conservation equations along the axial direction for each flux tube, that is the volume between to adjacent flux surfaces. In this way, we obtain an equality between the difference of upstream (west target, u) and downstream (east target, d) fluxes and all the remaining terms, which are treated as sources. Applying these ideas to equation (2) we obtain:

$$\mathrm{d}A_\perp \Gamma_x|_u^d = -\int_u^d \frac{1}{\sqrt{g}}\partial_y\left(\frac{\sqrt{g}}{h_y} n v_y\right)\sqrt{g}\mathrm{d}x\mathrm{d}y + \\ + \int_u^d S^n_{n,i}\sqrt{g}\mathrm{d}x\mathrm{d}y \tag{18}$$

where $\mathrm{d}A_\perp = h_y h_z \mathrm{d}y$ is the perpendicular cross-sectional area of the flux tube, and $\Gamma_x = b_x n v_x$. This procedure is performed for each flux tube and the resulting contribution are summed over, to obtain the total particle balance. The same is done also for the electron energy.

The graph on top of figure 7 shows with different colors each contribution on the right-hand side of equation (18), while the bottom graph represents the corresponding analysis for the electron energy balance, starting from equation (5).

From the density analysis, it can be noted that the strongest (positive) source term in the continuity equation is represented by the electron ionisation of neutral Ar atoms in Ar^+. Moreover, we can see that ionisation is stronly influenced by the external power absorbed by electrons: this source term (shown in light blue in the top part of figure 7) is almost constant for cases $a)-e)$, where the external ECR power is fixed at 800 W, and it increases significantly for case $f)$, where the external power is increased to 2400 W. Density and pressure-driven diffusions act instead as negative source terms. Recombination has not been reported since negligible in all simulations. Cases $a)$ - $e)$ show almost the same overall balance between ionisation and radial transport. Other slight differences that can be noted in the trends of figure 7 may be explained with reference to table 2. For example, lower and higher radial transport contribution shown in case $d)$ and $e)$ respectively, is consistent with the imposed values of D_n^{an} and D_p^{an}, also if compared to the reference case $a)$. On the other hand, case $c)$ shows higher ionisation, since more neutral atoms are present in the system to be ionised, due to lower pumping efficiency.

Similar considerations apply also for the electron energy balance, shown in figure 7 at the bottom. The strongest interactions for cases $a)-c)$ occurs with the neutral Ar atoms, while the remaining contributions play only a minor role. Specifically, cases $a)-e)$ show a rather similar energy balance. Case $f)$, where only the absorbed electron power was increased, is characterised by a strong boost in the the Ar^+ interaction term. This quantity includes all the electronic excitation of Ar^+ which ultimately leads to radiative losses and the ionisation of Ar^+ atoms to higher ionisation states, which was not included in the model.

5.3. Comparison with experimental results

A first comparison with experimentally available measured radial profiles of the electron density, temperature and plasma potential was performed, in order to test the capability of the code to reproduce both qualitatively and quantitatively the experimental data. The experimental data were taken with the following GyM configuration: *i*) coil currents fixed to 600 A; *ii*) gas puff intensity of 1 sccm of Ar; *iii*) RF power 1800 W.

For all the considered cases, n, T_e and ϕ are in the range of the experimental parameters of table 1. In all the simulations presented, the ion temperature is always below 0.2 eV, which is consistent with the fact that only the electrons are heated by the external power source and the low n, does not allow for an efficient energy equipartition.

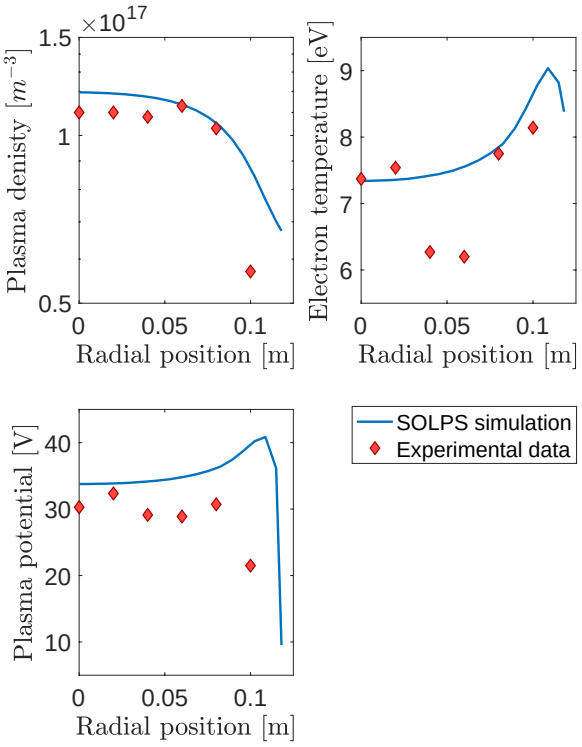

Figure 8. Radial profiles of the electron density, temperature and plasma potential, using the same input of case *a*) but with the absorbed power reduced to 400 W.

The comparison of the experimental points to the simulated radial profiles is shown in the bottom graph of figure 6. One can notice a good qualitative agreement between measurements and simulations. Firstly, the monotonic decreasing shape of the density profile is well captured. The simulated plasma potential slightly overestimates the increasing behaviour near the radial boundary with respect to the experimental profile. Finally, the behaviour of the experimental electron temperature is well captured by the simulations at the center and at the border of the machine, while the experimental dip around $r \simeq 0.05$ m is not properly reproduced. A possible explanation for this is related to the lack of a detailed modelling for the ECR source, which leads to the assumption of a radially constant absorption profile. A more detailed experimental campaign is planned, using a smaller spherical LP (2.5 mm radius) to enlarge the set of available experimental data both radially and axially. Moreover, a better investigation of the experimental uncertainty is needed, but from a first estimate values ~ 1 eV are consistent with the experimental technique used. Finally, dedicated studies on the RF wave propagation and absorption into the plasma should be considered.

Considering the bottom-left graph in figure 6, quantitative discrepancy is seen in the electron density up to a factor of 2, while the values of electron temperature and plasma potential are quite well captured. To better reproduce the density value at the axis, according to the results of the analysis reported in the previous section, we performed an additional simulation with the same parameters as for case *a*) of table 2, but we reduced the absorbed electron power to 400 W. Radial profiles of the electron density, temperature and plasma potential are shown in figure 8 and compared with experimental data. Here a satisfactory quantitative agreement between all simulated plasma quantities is clear. However, these good results concerning plasma quantities are obtained at the expenses of a factor ~ 20 discrepancy on the neutral pressure. Indeed, from the code we obtained a neutral pressure of $p_n = 2.78 \times 10^{-6}$ mbar, which strongly underestimates the experimental value of $p_{exp} = 54.6 \times 10^{-6}$ mbar. We address this issue in the following section.

5.4. EIRENE standalone simulations

In order to better investigate the discrepancy in the neutral pressure, we fixed the RECYCT coefficient with dedicated simulations. We used EIRENE in standalone mode to simulate the pre-plasma condition, providing to the code a background of Ar gas, with a negligible degree of ionization. In this way, the only code free parameter is the pumping surfaces albedo. To match the experimentally measured neutral pressure for a puffing strength of 1 sccm, the recycling coefficient of the pumping surfaces was set to RECYCT = 0.99682. Having fixed RECYCT to this value, the gas puff was then varied in the range $0.5 - 5$ sccm and the simulated neutral pressure at the gauge location shown in figure 5 compared with experimental data. Results are shown in figure 9. As can be seen,

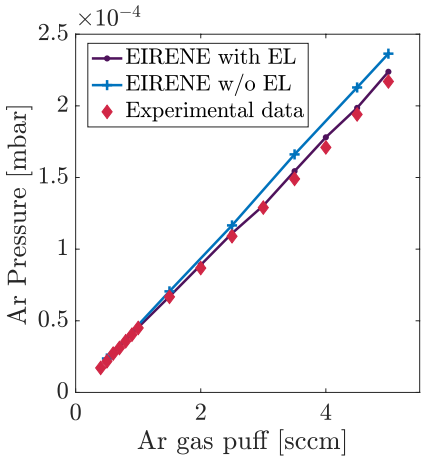

Figure 9. Neutral pressure at the gauge location for different values of the Ar puffing strength.

a good qualitative and quantitative agreement was obtained. For low gas-puff values (below 2.5 sccm), the simulated pressure (light blue line) shows a linear trend, in agreement with the experimental data (red diamonds). For higher values of the puffing strength, the experimental pressure is slightly below the simulated linear trend. This is due to the fact that our EIRENE model does not include neutral-neutral collisions. Additional simulations were thus performed including $Ar - Ar$ elastic collisions in the basic set of atomic reactions considered by EIRENE and treated with the BGK approximation [39]. As can be seen from the violet line figure 9 the inclusion of elastic $Ar - Ar$ allows to slightly decrease the simulated pressure, better recovering the experimental points. However, it should also be noted that no significant deviation occurs for 1 sccm of Ar, that is for the reference case that we considered in this work. The next step will be the adoption of the recycling coefficient fixed with the aforementioned procedure in B2.5-EIRENE coupled simulations. This will be the object of a future work.

6. Conclusions

The SOLPS-ITER code was applied in cylindrical geometry and for the simulations of Ar plasmas in the linear machine GyM. Non-hydrogenic plasmas are of great interest for PMI studies in LPDs. Furthermore, in its first phase, ITER will operate in pure Helium and thus these kind of simulations are of interest also in tokamak applications. Even though the code was developed to simulate the edge plasma in tokamaks, in this work we demonstrated that it can be also adapted to investigate the plasma behaviour in LPDs, obtaining results in satisfactory agreement with experimental data. We furthermore showed that pure Ar plasma can be simulated with SOLPS-ITER. This was by no means straightforward, since the code is meant for the simulation of H-dominated plasmas, where heavier species are treated as impurities as usually occurs in tokamaks.

Nevertheless, the analysis of the code equations highlighted that the physical model for non-hydrogenic plasmas is not complete and need further studies. Further perspectives of this work are related to the development of an integrated modelling for the study of PMI in LPDs. In this respect, Ar background plasmas retrieved from transport simulations will be used as input for material-specific codes such as ERO2.0 to study plasma induced modifications in the materials. Moreover, simulations of hydrogen or deuterium plasmas in GyM are foreseen. In the enriched picture which derives from the molecular nature of this gas, a tool like SOLPS-ITER becomes very important for the prediction of plasma composition in terms of atomic and molecular ions content. Being able to simulate plasma composition and particle, momentum and heat fluxes is the first step toward the development of a numerical integrated approach to interpret PMI experiments in LPDs.

Acknowledgments

This work has been carried out within the framework of the EUROfusion Consortium and has received funding from the Euratom research and training programme 2014-2018 and 2019-2020 under grant agreement No 633053. The views and opinions expressed herein do not necessarily reflect those of the European Commission or the ITER Organization.

References

[1] Schneider R *et al.* 2006 *Contributions to Plasma Physics* **46** 3–191
[2] Bufferand H *et al.* 2015 *Nuclear Fusion* **55** 053025
[3] Bufferand H *et al.* 2017 *Nuclear Materials and Energy* **12** 852 – 857 proceedings of the 22nd International Conference on Plasma Surface Interactions 2016, 22nd PSI
[4] Zhang D R *et al.* 2019 *Physics of Plasmas* **26** 012508
[5] Carli S *et al.* 2020 *Contributions to Plasma Physics* e201900155
[6] Baschetti S *et al.* 2019 *Nuclear Materials and Energy* **19** 200 – 204
[7] Zhang C *et al.* 2019 *Plasma Physics and Controlled Fusion* **61** 115013
[8] Si H *et al.* 2019 *Plasma Physics and Controlled Fusion* **61** 095007
[9] Chen J *et al.* 2019 *Physics of Plasmas* **26** 052501
[10] Senichenkov I *et al.* 2019 *Plasma Physics and Controlled Fusion* **61** 045013
[11] Brezinsek S *et al.* 2017 *Nuclear Fusion* **57** 116041
[12] Pezzoli A *et al.* 2015 *Journal of Nuclear Materials* **463** 1041–1044
[13] Kastelewicz H and Fussmann G 2004 *Contributions to Plasma Physics* **44** 352–360
[14] Baeva M *et al.* 2007 *Journal of Nuclear Materials* **363-365** 330–334
[15] Rapp J *et al.* 2015 *Journal of Nuclear Materials* **463** 510–514
[16] Owen L W *et al.* 2017 *Physics of Plasmas* **24** 112504
[17] Kafle N *et al.* 2018 *Physics of Plasmas* **25** 052508
[18] Owen L W *et al.* 2017 *Plasma Sources Science and Technology* **26** 055005
[19] Ješko K *et al.* 2018 *Plasma Physics and Controlled Fusion* **60** 125009
[20] Ješko K *et al.* 2018 *Contributions to Plasma Physics* **58** 798–804
[21] Stangeby P 2000 *The Plasma Boundary of Magnetic Fusion Devices* Series in Plasma Physics and Fluid Dynamics (Taylor & Francis) ISBN 9780750305594
[22] Kotov V and Reiter D 2009 *Plasma Physics and Controlled Fusion* **51** 115002
[23] Takeda H *et al.* 2013 *Fusion Science and Technology* **63** 414–416
[24] Islam M S, Nakashima Y and Hatayama A 2017 *Plasma Physics and Controlled Fusion* **59** 125010
[25] Islam S M *et al.* 2018 *Contributions to Plasma Physics* **58** 805–811
[26] Takechi S *et al.* 2019 *Plasma and Fusion Research* **14** 2403045
[27] Islam M S *et al.* 2019 *Nuclear Materials and Energy* **18** 182–187
[28] Rogers B *et al.* 2010 *Phys. Rev. Lett.* **104**(22) 225002
[29] Fisher D M and Rogers B N 2017 *Physics of Plasmas* **24** 022303
[30] Løiten M 2017 *Global numerical modeling of magnetized plasma in a linear device* Ph.D. thesis Technical University of Denmark
[31] Leddy J, Dudson B and Willett H 2017 *Nuclear Materials and Energy* **12** 994 – 998 proceedings of the 22nd International Conference on Plasma Surface Interactions 2016, 22nd PSI
[32] Leddy J and Dudson B 2017 *Plasma Physics and Controlled Fusion* **59** 125011
[33] Iraji D *et al.* 2012 *Fusion Science and Technology* **62** 428–435
[34] Laguardia L *et al.* 2015 *Journal of Nuclear Materials* **463** 680–683
[35] Dong L *et al.* 2018 *Plasma Science and Technology* **20** 065102
[36] Kallenbach A *et al.* 2013 *Plasma Physics and Controlled Fusion* **55** 124041
[37] Eksaeva A *et al.* 2017 *Nuclear Materials and Energy* **12** 253–260
[38] Marenkov E *et al.* 2015 *Journal of Nuclear Materials* **463** 268–271
[39] Eirene manual http://www.eirene.de/manuals/eirene.pdf
[40] Baelmans M 1993 Code improvements and applications of a two-dimensional edge plasma model for toroidal fusion devices https://lirias.kuleuven.be/retrieve/373852
[41] Rozhansky V *et al.* 2009 *Nuclear Fusion* **49** 025007
[42] Zhdanov V 2002 *Transport Processes in Multicomponent Plasma* vol 44
[43] Dekeyser W *et al.* B2–b2.5 code benchmarking http://www.eirene.de/Juel_4337_Reiter.pdf
[44] Sytova E *et al.* 2018 *Contributions to Plasma Physics* **58** 622–628
[45] Rozhansky V *et al.* 2001 *Nuclear Fusion* **41** 387–401
[46] Jeon Y 2015 *Journal of the Korean Physical Society* **67** 843–853
[47] Baelmans M, Börner P, Dekeyser W and Reiter D 2011 *Nuclear Fusion* **51** 083023
[48] Fundamenski W 2005 *Plasma Physics and Controlled Fusion* **47** R163–R208
[49] Manz P *et al.* 2020 *Physics of Plasmas* **27** 022506